CELL BIOLOGY

ANT-dependent MPTP underlies necrotic myofiber death in muscular dystrophy

Michael J. Bround[1], Julian R. Havens[1], Allen J. York[1], Michelle A. Sargent[1], Jason Karch[2], Jeffery D. Molkentin[1]*

Mitochondrial permeability transition pore (MPTP) formation contributes to ischemia-reperfusion injury in the heart and several degenerative diseases, including muscular dystrophy (MD). MD is a family of genetic disorders characterized by progressive muscle necrosis and premature death. It has been proposed that the MPTP has two molecular components, the adenine nucleotide translocase (ANT) family of proteins and an unknown component that requires the chaperone cyclophilin D (CypD) to activate. This model was examined in vivo by deleting the gene encoding ANT1 (*Slc25a4*) or CypD (*Ppif*) in a δ-sarcoglycan (*Sgcd*) gene–deleted mouse model of MD, revealing that dystrophic mice lacking *Slc25a4* were partially protected from cell death and MD pathology. Dystrophic mice lacking both *Slc25a4* and *Ppif* together were almost completely protected from necrotic cell death and MD disease. This study provides direct evidence that ANT1 and CypD are required MPTP components governing in vivo cell death, suggesting a previously unrecognized therapeutic approach in MD and other necrotic diseases.

INTRODUCTION

The mitochondrial permeability transition pore (MPTP) is a megachannel in the inner mitochondrial membrane that opens in response to high matrix Ca^{2+} and oxidative stress (*1*). MPTP activation permeabilizes the inner mitochondrial membrane to solutes of up to 1.5 kDa, induces mitochondrial swelling and membrane rupture, dissolves the adenosine triphosphate (ATP) producing H^+ gradient, and initiates necrotic cell death (*2*). MPTP-dependent cell death contributes to several important human diseases including cardiac ischemia-reperfusion injury, muscular dystrophy (MD), and neurodegenerative diseases such as Huntington's disease, amyotrophic lateral sclerosis, and Alzheimer's disease (*3*–*10*).

Despite a wealth of data describing the MPTP phenomenon, the molecular identity of the MPTP itself remains controversial (*1*). One of the early proposed molecular candidates for the MPTP was the adenine nucleotide translocase (ANT) family of proteins (*11*, *12*); however, genetic experiments were less definitive (*13*). We revisited this model and observed that the ANT family of proteins do comprise one part of the MPTP (*14*). Specifically, deletion of the three mouse ANT isoform encoding genes resulted in desensitization of the MPTP, although activation was not blocked (*14*). However, when liver mitochondria lacking all three ANT isoforms were also treated with cyclosporin A (CsA), an inhibitor of the MPTP regulatory protein cyclophilin D (CypD) (*15*–*18*), MPTP activation was abolished (*14*). Simultaneous deletion of *Ppif* (CypD gene) with the three ANT isoform encoding genes also abolished MPTP opening (*14*). These results suggested that the MPTP is composed of ANT and another unknown protein species that requires CypD (*14*, *19*). The mitochondrial ATP synthase complex may also generate MPTP-like activity, either at the level of the c-ring subunit within the adenosine triphosphatase (ATPase) core or at the interface between the ATPase core and the oligomycin sensitivity conferral protein (OSCP) subunit (*20*, *21*). A recent study of ATP synthase c-subunit–deleted mitochondria displayed a substantial change in MPTP conductance but retained a smaller MPTP-like pore that could be inhibited by the ANT-specific antagonist bongkrekic acid (BKA) (*22*). Another study testing the role of ATPase subunits in MPTP found that genetic ablation of the OSCP, b, and g ATPase subunits in HeLa cells caused altered CsA-sensitive MPTP activity but retained ANT-dependent MPTP activity that could be induced by atractyloside, an ANT-specific MPTP-sensitizing agent, or inhibited by BKA (*23*). A recent proteomics study of the mitochondrial interactome in the failing heart identified an ANT1 species that is consistent with an open pore-forming conformation providing evidence that ANT proteins form MPTP pores in a pathophysiological context (*24*). Collectively, these studies provide evidence for ANT-dependent, two-component model of the MPTP. However, the role of ANT-dependent MPTP has only been investigated in reductionist systems, so it remains unclear whether it serves as a bona fide regulator of necrotic cell death in vivo.

MD is a family of genetic disorders characterized by progressive muscle wasting, decreased muscle function, and premature death (*25*). At the myofiber level, many sMD result in sarcolemma instability and rupture resulting in uncontrolled Ca^{2+} influx leading to myofiber necrotic cell death and progressive pathology (*26*). Previous studies have demonstrated that genetic or pharmacological inhibition of CypD reduces myofiber cell death and decreases MD disease burden in animal models (*5*, *27*–*29*). Here, we generated $Slc25a4^{-/-}$ (ANT1 protein) mice as well as mice deficient in both $Slc25a4^{-/-}$ and $Ppif^{-/-}$ (CypD protein), which when crossed into the δ-sarcoglycan gene deletion ($Sgcd^{-/-}$) mouse model of MD (*30*) leads to a stepwise reduction in myofiber necrosis and MD disease manifestation. These results indicate that the ANT-dependent component of the MPTP underlies necrotic cell death in vivo. Furthermore, because simultaneous deletion of *Slc25a4* with *Ppif* caused an almost complete inhibition of muscle histopathology in

---

[1]Department of Pediatrics, Cincinnati Children's Hospital and the University of Cincinnati, Cincinnati, OH, USA. [2]Department of Integrative Physiology, Baylor College of Medicine, Houston, TX, USA.
*Corresponding author. Email: jeff.molkentin@cchmc.org

these *Sgcd*$^{-/-}$ mice, it supports the two-component model of the MPTP as contributing to necrosis in a disease relevant model.

RESULTS

Mitochondria-dependent myofiber necrosis is a major underlying mechanism leading to pathology in MD. To assess MPTP activity in dystrophic mitochondria, we simultaneously measured the Ca^{2+} retention capacity (CRC) and absorbance-based swelling in mitochondria isolated from either healthy wild-type (WT) muscle or *Sgcd*$^{-/-}$ dystrophic muscle (*30*). We observed that *Sgcd*$^{-/-}$ myofiber mitochondria exhibited substantially reduced CRC compared with WT mitochondria (Fig. 1A), as has been observed in isolated skeletal muscle mitochondria from *mdx* mice, a model of Duchenne MD (*31*). We also observed that mitochondria from quadricep of *Sgcd*$^{-/-}$ mice released more Ca^{2+} than WT mitochondria, which suggests that dystrophic mitochondria are in a state of Ca^{2+} overload (Fig. 1B). This increase in matrix Ca^{2+} is known to cause the increased MPTP activation that underlies myofiber necrosis in dystrophic muscle, as mice lacking the *Ppif* gene are partially protected (*5*, *28*).

To interrogate the role and identity of the MPTP in MD pathology, we investigated mice with genetic deletion of the genes encoding the ANT isoforms. Healthy skeletal muscle almost exclusively expresses *Slc25a4* (ANT1), and previous studies of *Slc25a4* gene–deleted mice did not show up-regulation of *Slc25a5* (ANT2) expression in skeletal muscle (*32*, *33*). However, *Slc25a5* expression was shown to be up-regulated in the muscles of *mdx* mice (*31*), suggesting that it may contribute to MD pathology. Accordingly, here, we generated *Slc25a4* gene–deleted mice crossed into the δ-sarcoglycan

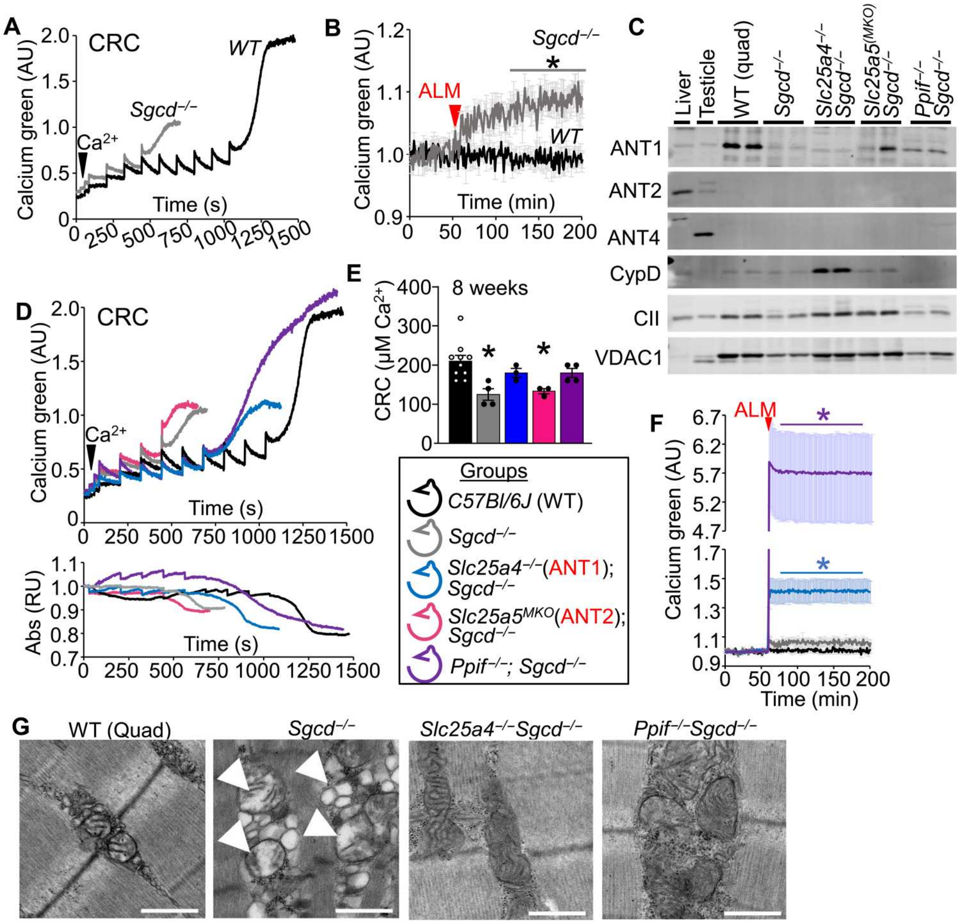

Fig. 1. *Slc25a4* gene deletion desensitizes MPTP activity in dystrophic muscle. (**A**) Representative mitochondrial CRC assay of isolated *C57Bl/6J* WT and *Sgcd*$^{-/-}$ quadricep mitochondria. The arrow and each inflection point represent 20 μM additions of CaCl$_2$. The *y* axis is arbitrary units (AU). (**B**) Mitochondrial Ca^{2+} overload assay of isolated WT and *Sgcd*$^{-/-}$ quadricep mitochondria. Two milligrams of mitochondria was treated with 40 μM alamethicin (ALM, red arrow). WT $n = 4$; *Sgcd*$^{-/-}$ $n = 3$ ($^*P \leq 0.05$ versus WT). The *y* axis is arbitrary units. (**C**) Western blots of quadricep mitochondria for the proteins: ANT1, ANT2, ANT4, CypD, and the protein-loading controls electron transport chain complex II (CII) and voltage-dependent anion channel 1 (VDAC1). Testis is a positive control for ANT4 and liver for ANT2. (**D**) Representative mitochondrial CRC assay (top) and simultaneous swelling (bottom) as absorption (Abs) in relative units (RU) with (**E**) average CRC measurements of isolated quadricep mitochondria from the indicated genotypes of mice. The *y* axis is arbitrary units. The legend shows genotypes of mice used by color coding in the figure panels. WT $n = 10$; *Sgcd*$^{-/-}$ $n = 4$; *Slc25a4*$^{-/-}$;*Sgcd*$^{-/-}$ $n = 3$; *Slc25a5*^{MKO};*Sgcd*$^{-/-}$, $n = 3$; *Ppif*$^{-/-}$;*Sgcd*$^{-/-}$, $n = 4$ ($^*P \leq 0.05$ versus WT). (**F**) Mitochondrial Ca^{2+} load assay from quadricep of the indicated genotypes of mice. Forty micromolar alamethicin was used. The *y* axis is arbitrary units. WT $n = 6$; *Sgcd*$^{-/-}$ $n = 3$; *Slc25a4*$^{-/-}$;*Sgcd*$^{-/-}$ $n = 15$; *Ppif*$^{-/-}$;*Sgcd*$^{-/-}$ $n = 8$ ($^*P \leq 0.05$ versus WT). (**G**) Representative transmission electron micrographs of quadricep from mice with the indicated genotypes. Scale bar, 800 nm. White arrows indicate swollen mitochondria with few cristae.

model of limb-girdle MD (*Slc25a4*$^{-/-}$;*Sgcd*$^{-/-}$) (*30*). We also analyzed mice with muscle-specific deletion of the *Slc25a5* gene [LoxP (fl) targeted] using the *Myl1*^{Cre}*-allele* herein called *Slc25a5*^{MKO} [germline loss of *Slc25a5* in mice is embryonic lethal (*34*)]. We investigated the previously published *Ppif*$^{-/-}$ (CypD) gene deleted mice (*Ppif*$^{-/-}$;*Sgcd*$^{-/-}$) in the same dystrophic background for direct experimental comparison (*5*). All mouse models were viable, and there was no difference in total body weight between groups (Fig. 1C and fig. S1A), although muscle weights changed on the basis of the degree of ongoing dystrophic damage (fig. S1, B to E), see below.

Analysis of protein expression in isolated quadricep mitochondria showed a complete loss of ANT1 protein in *Slc25a4*$^{-/-}$;*Sgcd*$^{-/-}$ mice, without an increase in ANT2 or ANT4 expression (Fig. 1C). However, we did observe an increase in CypD protein levels in *Slc25a4*$^{-/-}$;*Sgcd*$^{-/-}$ mitochondria isolated from quadriceps (Fig. 1C). We also observed an increase in CypD protein in nondsytrophic *Slc25a4*$^{-/-}$ quadriceps mitochondria, as well as an increase in ANT1 protein in nondystrophic *Ppif*$^{-/-}$ quadriceps mitochondria, suggesting potential compensation between these two effectors in regulating MPTP activity (fig. S2A). ANT2 protein was not observed in isolated mitochondria from adult WT or *Sgcd*$^{-/-}$ quadricep (Fig. 1C).

Muscle mitochondria from these same groups of mice were assessed for CRC and absorbance-based mitochondrial swelling. We observed that quadricep-derived mitochondria from *Slc25a4*$^{-/-}$;*Sgcd*$^{-/-}$ mice had increased CRC and delayed swelling compared to *Sgcd*$^{-/-}$ mitochondria (Fig. 1, D and E), suggesting that MPTP activation is desensitized compared to mitochondria from *Sgcd*$^{-/-}$ muscle. *Slc25a4*$^{-/-}$;*Sgcd*$^{-/-}$ mitochondria CRC levels and swelling were indistinguishable from *Ppif*$^{-/-}$;*Sgcd*$^{-/-}$ mitochondria, demonstrating that *Slc25a4* gene deletion yielded similar MPTP desensitization to *Ppif* gene deletion as previously reported (*5*). Consistent with the lack of ANT2 protein expression in mouse skeletal muscle, CRC and swelling in isolated mitochondria from *Slc25a5*^{MKO};*Sgcd*$^{-/-}$ muscle were identical to *Sgcd*$^{-/-}$ mitochondria (Fig. 1, D and E). Direct analysis of mitochondrial matrix Ca^{2+} in quadricep from these groups showed that both *Slc25a4*$^{-/-}$;*Sgcd*$^{-/-}$ and *Ppif*$^{-/-}$;*Sgcd*$^{-/-}$ mice released significantly more Ca^{2+} than either WT or *Sgcd*$^{-/-}$ muscle mitochondria (Fig. 1F), suggesting some degree of mitochondrial Ca^{2+} overload despite MPTP desensitization. This result suggests the CRC experiments (Fig. 1, D and E) likely underestimate the degree of muscle MPTP desensitization in *Slc25a4*$^{-/-}$;*Sgcd*$^{-/-}$ and *Ppif*$^{-/-}$;*Sgcd*$^{-/-}$ mice.

To assess the in vivo status of *Slc25a4*$^{-/-}$;*Sgcd*$^{-/-}$ mitochondria, we performed transmission electron microscopy of quadricep muscle. As expected, intramuscle mitochondria from *Sgcd*$^{-/-}$ mice showed swelling, disorganized cristae, and loss of membrane integrity (Fig. 1G). However, electron micrographs from quadriceps of both *Slc25a4*$^{-/-}$;*Sgcd*$^{-/-}$ and *Ppif*$^{-/-}$;*Sgcd*$^{-/-}$ mice showed improved mitochondria morphology, albeit with some baseline swelling. We also assessed mitochondrial metabolic function using a Seahorse bioanalyzer and found that *Sgcd*$^{-/-}$ quadricep mitochondria had significantly reduced maximal oxygen consumption rates (OCRs) compared to WT mitochondria (fig. S2B). Unexpectedly, *Slc25a4*$^{-/-}$;*Sgcd*$^{-/-}$ but not *Ppif*$^{-/-}$;*Sgcd*$^{-/-}$ mitochondria had maximal OCR rates restored to WT levels under optimal metabolic substrate conditions (fig. S2B). Collectively, these results demonstrate that *Slc25a4* (ANT1) gene deletion desensitizes MPTP activation and improves mitochondrial function in vivo in skeletal muscle with MD.

Quadricep-derived mitochondria from *Ppif*$^{-/-}$;*Sgcd*$^{-/-}$ mice released significantly more Ca^{2+} than *Slc25a4*$^{-/-}$;*Sgcd*$^{-/-}$ mitochondria (Fig. 1F). We therefore measured the CRC of quadricep-derived mitochondria from nondystrophic *Slc25a4*$^{-/-}$ and *Ppif*$^{-/-}$ mice and observed that while *Slc25a4*$^{-/-}$ mitochondria had greater CRC than WT control mitochondria, they had significantly less CRC than *Ppif*$^{-/-}$ mitochondria (fig. S2, C and D). These data suggest that the mitochondrial Ca^{2+} content observed in dystrophic mitochondria is due to differences in overall CRC capacity between these groups. To further investigate the greater levels of quadricep mitochondrial Ca^{2+} released from *Ppif*$^{-/-}$;*Sgcd*$^{-/-}$ mice, we performed Western blotting for the Ca^{2+} handling effectors of the mitochondrial Ca^{2+} uniporter (MCU) complex. We observed that mitochondria from *Slc25a4*$^{-/-}$;*Sgcd*$^{-/-}$ mice had increased levels of the dominant-negative MCU-complex subunit MCUb, as well as the MCU-complex gatekeeping protein MICU1 compared to *Sgcd*$^{-/-}$ mitochondria (fig. S2E). Conversely, quadricep mitochondria from *Ppif*$^{-/-}$;*Sgcd*$^{-/-}$ mice do not show increased levels of MCUb and low levels of MICU1, despite maintaining a robust level of MCU expression (fig. S2E). Both a reduction of MCUb (*35*, *36*), and a decrease in the ratio of MICU1:MCU (*37*) are consistent with a more active MCU complex. This suggests that *Ppif*$^{-/-}$;*Sgcd*$^{-/-}$ mitochondria, but not *Slc25a4*$^{-/-}$;*Sgcd*$^{-/-}$ mitochondria, have a larger CRC and greater mitochondrial Ca^{2+} uptake, which likely underlies the markedly increased Ca^{2+} levels observed in the *Ppif*$^{-/-}$;*Sgcd*$^{-/-}$ mitochondria (Fig. 1F).

To determine whether ANT-dependent MPTP formation contributed to in vivo necrosis in MD, we assessed several aspects of MD pathophysiology in these models. As alluded to above, we observed that pseudo-hypertrophy for the tibialis anterior (TA) and quadricep was reduced in *Slc25a4*$^{-/-}$;*Sgcd*$^{-/-}$ and *Ppif*$^{-/-}$;*Sgcd*$^{-/-}$ mice compared with *Sgcd*$^{-/-}$ controls at 16 weeks of age, although there was no difference at 8 weeks (fig. S1, B to E). Histological analysis revealed that diaphragms and quadriceps from *Slc25a4*$^{-/-}$;*Sgcd*$^{-/-}$ mice displayed substantially less pathology than *Sgcd*$^{-/-}$ control or *Slc25a5*^{MKO};*Sgcd*$^{-/-}$ mice (Fig. 2A and fig. S3A). Specifically, diaphragms and quadriceps from *Slc25a4*$^{-/-}$;*Sgcd*$^{-/-}$ mice did not have large expanding necrotic zones and instead had small localized regions of muscle fiber death. The same type of small localized fiber death was observed in *Ppif*$^{-/-}$;*Sgcd*$^{-/-}$ muscle, while muscles from *Slc25a5*^{MKO};*Sgcd*$^{-/-}$ mice had large necrotic regions similar to *Sgcd*$^{-/-}$ mice. Combinatorial deleted *Slc25a4*$^{-/-}$;*Slc25a5*^{MKO};*Sgcd*$^{-/-}$ (ANT1 and ANT2) mice and *Slc25a4*$^{-/-}$;*Slc25a31*;*Sgcd*$^{-/-}$ (ANT1 and ANT4) mice showed the same amount of histopathology and myofiber central nucleation as *Slc25a4*$^{-/-}$;*Sgcd*$^{-/-}$ mice (fig. S3, A and B), indicating that additionally targeting the ANT2 or ANT4 encoding genes did not alter necrosis in MD beyond the effect of ANT1 loss. Consistent with this, there was no additional increase in CRC in *Slc25a4*$^{-/-}$;*Slc25a5*^{MKO};*Sgcd*$^{-/-}$ or *Slc25a4*$^{-/-}$;*Slc25a31*;*Sgcd*$^{-/-}$ isolated muscle mitochondria versus *Slc25a4*$^{-/-}$;*Sgcd*$^{-/-}$ (fig. S3, C and D).

To better characterize the degree of MD protection associated with *Slc25a4* deletion, we quantified the rate of myofiber central nucleation and observed that quadricep from *Slc25a4*$^{-/-}$;*Sgcd*$^{-/-}$ mice had increased levels compared with WT but significantly less than

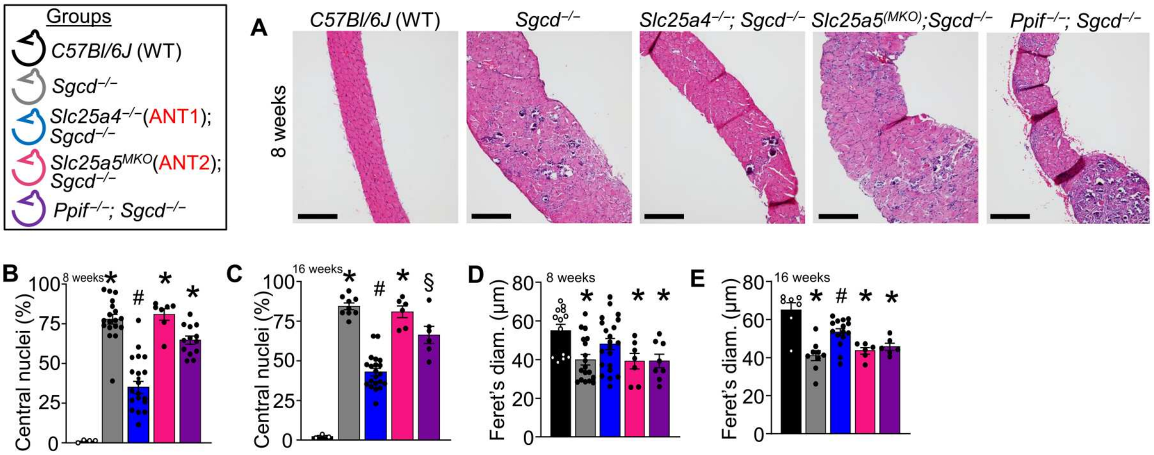

Fig. 2. *Slc25a4* (ANT1) gene deletion reduces histopathology in MD. (**A**) Representative hematoxylin and eosin (H&E)–stained diaphragm sections from 8-week-old mice of the indicated genotypes. Scale bar, 200 μm. (**B**) Quantification of myofiber central nucleation in quadricep sections from 8-week-old mice of the indicated genotypes of mice in the legend by color coding. WT $n = 4$; *Sgcd*$^{-/-}$ $n = 18$; *Slc25a4*$^{-/-}$;*Sgcd*$^{-/-}$ $n = 22$; *Slc25a5*^{MKO};*Sgcd*$^{-/-}$, $n = 7$; *Ppif*$^{-/-}$;*Sgcd*$^{-/-}$ $n = 13$ (*$P \leq 0.05$ versus WT; #$P \leq 0.05$ versus WT and *Sgcd*$^{-/-}$). (**C**) Quantification of myofiber central nucleation in quadricep sections from 16-week-old mice. WT $n = 3$; *Sgcd*$^{-/-}$ $n = 9$; *Slc25a4*$^{-/-}$;*Sgcd*$^{-/-}$ $n = 21$; *Slc25a5*^{MKO};*Sgcd*$^{-/-}$, $n = 6$; *Ppif*$^{-/-}$;*Sgcd*$^{-/-}$ $n = 6$ (*$P \leq 0.05$ versus WT; #$P \leq 0.05$ versus WT and *Sgcd*$^{-/-}$; §$P \leq 0.05$ versus WT, Sgcd$^{-/-}$, and *Slc25a4*$^{-/-}$;*Sgcd*$^{-/-}$). (**D**) Average Feret's diameter of quadricep myofibers in sections from 8-week-old mice of the indicated genotypes. WT $n = 13$; *Sgcd*$^{-/-}$ $n = 18$; *Slc25a4*$^{-/-}$;*Sgcd*$^{-/-}$ $n = 21$; *Slc25a5*^{MKO};*Sgcd*$^{-/-}$, $n = 7$; *Ppif*$^{-/-}$;*Sgcd*$^{-/-}$ $n = 8$ (*$P \leq 0.05$ versus WT). (**E**) Average Feret's diameter of quadricep myofibers in sections from 16-week-old mice of the indicated genotypes. WT $n = 7$; *Sgcd*$^{-/-}$ $n = 9$; *Slc25a4*$^{-/-}$;*Sgcd*$^{-/-}$ $n = 15$; *Slc25a5*^{MKO};*Sgcd*$^{-/-}$, $n = 6$; *Ppif*$^{-/-}$;*Sgcd*$^{-/-}$ $n = 6$ (*$P \leq 0.05$ versus WT; #$P \leq 0.05$ versus WT and *Sgcd*$^{-/-}$).

Sgcd$^{-/-}$ or *Slc25a5*^{MKO};*Sgcd*$^{-/-}$ mice at both 8 and 16 weeks of age (Fig. 2, B and C). Central nucleation in *Slc25a4*$^{-/-}$;*Sgcd*$^{-/-}$ quadricep was also significantly lower than in *Ppif*$^{-/-}$;*Sgcd*$^{-/-}$ muscle, suggesting that *Slc25a4* gene deletion may be more protective than *Ppif* gene deletion in MD. Consistent with this, we observed that *Slc25a4*$^{-/-}$;*Sgcd*$^{-/-}$ quadricep had partially preserved myofiber size that was not observed in *Ppif*$^{-/-}$;*Sgcd*$^{-/-}$ muscle (Fig. 2, D and E). Both *Slc25a4*$^{-/-}$;*Sgcd*$^{-/-}$ and *Ppif*$^{-/-}$;*Sgcd*$^{-/-}$ quadriceps displayed significantly reduced embryonic myosin heavy chain (Myh3) expression (Fig. 3, A and B), which is another indicator of reduced myofiber degeneration-regeneration. Similarly, both *Slc25a4*$^{-/-}$;*Sgcd*$^{-/-}$ and *Ppif*$^{-/-}$;*Sgcd*$^{-/-}$ quadriceps showed lower rates of acute Evan's blue dye (EBD) uptake following a downhill treadmill challenge compared with *Sgcd*$^{-/-}$ or *Slc25a5*^{MKO};*Sgcd*$^{-/-}$ mice, demonstrating increased myofiber membrane stability (Fig. 3C). Changes in muscle histology, central nucleation, or myofiber size were not observed in nondystrophic *Slc25a4*$^{-/-}$ or *Ppif*$^{-/-}$ control animals (fig. S4, A to C). Collectively, these data demonstrate that *Slc25a4* (ANT1) gene deletion reduces MD pathology and in vivo necrosis.

The impact of *Slc25a4* gene deletion on muscle performance in MD was examined. *Sgcd*$^{-/-}$ dystrophic mice ran a significantly shorter distance before exhaustion on a treadmill compared with WT mice at 8 and 16 weeks of age (Fig. 3, D and E). *Slc25a4*$^{-/-}$;*Sgcd*$^{-/-}$ and *Ppif*$^{-/-}$;*Sgcd*$^{-/-}$ mice ran significantly further than *Sgcd*$^{-/-}$ control animals (Fig. 3, D and E), however neither group were able to complete the running protocol unlike healthy WT mice (Fig. 3, D and E). This is likely due to metabolic dysfunction as *Slc25a4* gene deletion causes exercise intolerance and mitochondrial myopathy in mice and humans (*32*, *38*, *39*), and *Ppif* gene deletion in mice causes cardiac metabolic dysfunction and vulnerability to cardiac stress (*40*). Both nondystrophic *Slc25a4*$^{-/-}$ and *Ppif*$^{-/-}$ control animals struggle to complete the downhill treadmill running protocol in contrast to WT mice (fig. S4D). These experiments reveal that while *Slc25a4* (ANT1) gene deletion reduces MD pathology and provides some functional muscle improvement, metabolic exercise intolerance likely prevents greater rescue of muscle performance.

In our previous cell-reductionist work, we observed that the full extent of MPTP activity required ANT and another component separately regulated by CypD (*14*). Here, we observed that CypD protein levels were substantially increased in *Slc25a4*$^{-/-}$ mitochondria from dystrophic muscle, consistent with this dual regulation model (Fig. 1C and fig S2A). Skeletal muscle mitochondria from *Slc25a4*$^{-/-}$;*Sgcd*$^{-/-}$ mice showed a synergistically greater CRC when treated with CsA to inhibit CypD, and mitochondrial swelling was similarly desensitized (Fig. 4, A and B). We therefore examined mice in which the *Slc25a4* gene was deleted in combination with the *Ppif* gene in the *Sgcd*$^{-/-}$ background. Consistent with these results, mitochondria isolated from skeletal muscle of *Slc25a4*$^{-/-}$;*Ppif*$^{-/-}$;*Sgcd*$^{-/-}$ mice demonstrated the same synergistic increase in CRC and swelling desensitization as the CsA-treated *Slc25a4*$^{-/-}$;*Sgcd*$^{-/-}$ muscle mitochondria (Fig. 4, A and B). Analysis of matrix Ca^{2+} release from *Slc25a4*$^{-/-}$;*Ppif*$^{-/-}$;*Sgcd*$^{-/-}$ muscle mitochondria was markedly higher compared with WT or *Sgcd*$^{-/-}$ muscle-derived mitochondria (Fig. 4C). This indicates that *Slc25a4*$^{-/-}$;*Ppif*$^{-/-}$;*Sgcd*$^{-/-}$ mitochondria are in a state of Ca^{2+} overload and that the CRC data likely under-represent the true desensitization of the MPTP, which is almost completely inhibited.

In vivo examination of skeletal muscle from *Slc25a4*$^{-/-}$;*Ppif*$^{-/-}$;*Sgcd*$^{-/-}$ mice by transmission electron microscopy revealed the same state of mitochondrial swelling observed in *Slc25a4*$^{-/-}$;*Sgcd*$^{-/-}$ and *Ppif*$^{-/-}$;*Sgcd*$^{-/-}$ mice but with substantially improved morphology, cristae organization, and membrane integrity compared to *Sgcd*$^{-/-}$ dystrophic mitochondria (Fig. 4D). Unexpectedly, we observed that quadricep mitochondria from

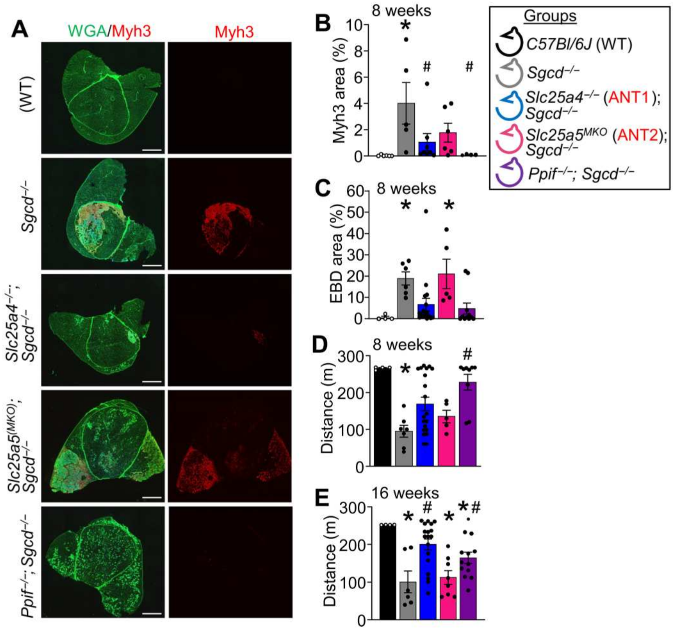

Fig. 3. *Slc25a4* (ANT1) gene deletion reduces muscle degeneration in MD. (**A**) Quadricep sections immunostained for embryonic myosin heavy chain (Myh3; red) and costained with wheat germ agglutinin (WGA; green) from 8-week-old mice of the indicated genotypes. Scale bar, 1 mm. (**B**) Quantification of Myh3^{+} area in quadricep sections in 8-week-old mice of the indicated genotypes. WT $n = 6$; *Sgcd*$^{-/-}$ $n = 5$; *Slc25a4*$^{-/-}$;*Sgcd*$^{-/-}$ $n = 8$; *Slc25a5*^{MKO};*Sgcd*$^{-/-}$, $n = 6$; *Ppif*$^{-/-}$;*Sgcd*$^{-/-}$ $n = 4$ (*$P \leq 0.05$ versus WT; #$P \leq 0.05$ versus *Sgcd*$^{-/-}$). (**C**) Quantification of EBD-positive area in quadricep sections in 8-week-old mice of the indicated genotypes. WT $n = 4$; *Sgcd*$^{-/-}$ $n = 6$; *Slc25a4*$^{-/-}$;*Sgcd*$^{-/-}$ $n = 17$; *Slc25a5*^{MKO};*Sgcd*$^{-/-}$, $n = 5$; *Ppif*$^{-/-}$;*Sgcd*$^{-/-}$ $n = 11$ (*$P \leq 0.05$ versus WT). (**D**) Average treadmill running distance in meters for 8-week-old mice of the indicated genotypes. Maximum possible running distance is 270 m. WT $n = 4$; *Sgcd*$^{-/-}$ $n = 7$; *Slc25a4*$^{-/-}$;*Sgcd*$^{-/-}$ $n = 20$; *Slc25a5*^{MKO};*Sgcd*$^{-/-}$, $n = 5$; *Ppif*$^{-/-}$;*Sgcd*$^{-/-}$ $n = 9$ (*$P \leq 0.05$ versus WT; #$P \leq 0.05$ versus *Sgcd*$^{-/-}$). (**E**) Average treadmill running distance in meters for 16-week-old mice of the indicated genotypes. WT $n = 4$; *Sgcd*$^{-/-}$ $n = 6$; *Slc25a4*$^{-/-}$;*Sgcd*$^{-/-}$ $n = 18$; *Slc25a5*^{MKO};*Sgcd*$^{-/-}$, $n = 8$; *Ppif*$^{-/-}$;*Sgcd*$^{-/-}$ $n = 13$ (*$P \leq 0.05$ versus WT; #$P \leq 0.05$ versus *Sgcd*$^{-/-}$).

Slc25a4$^{-/-}$;*Ppif*$^{-/-}$;*Sgcd*$^{-/-}$ mice uniquely showed up-regulation of ANT2 protein (Fig. 4E, red box), suggesting potential metabolic compensation. Measurement of mitochondrial respiration using a Seahorse analyzer showed reduced capacity in *Sgcd*$^{-/-}$ mitochondria compared with WT but that mitochondria from quadricep of *Slc25a4*$^{-/-}$;*Ppif*$^{-/-}$;*Sgcd*$^{-/-}$ mice had rescued maximal respiration under ideal substrate conditions (Fig. 4F). Collectively, these experiments show that combined *Slc25a4* (ANT1) and *Ppif* (CypD) gene deletion causes a "synergistic" desensitization of MPTP opening not observed in muscle from either *Slc25a4*$^{-/-}$;*Sgcd*$^{-/-}$ or *Ppif*$^{-/-}$;*Sgcd*$^{-/-}$ mice. The unique induction of the ANT2 expression by double deletion of ANT1 and CypD encoding genes likely explains the enhanced metabolic function and other improvements (see below).

The electron micrographs from *Slc25a4*$^{-/-}$;*Ppif*$^{-/-}$;*Sgcd*$^{-/-}$ mice appeared to show an expansion both in the number and size of quadricep mitochondria compared to both *Sgcd*$^{-/-}$ and WT controls (Fig. 4D). We therefore quantified mitochondrial DNA (mtDNA) content and observed reductions in mtDNA from *Sgcd*$^{-/-}$ quadricep compared to WT, but that muscle from both *Slc25a4*$^{-/-}$ and *Slc25a4*$^{-/-}$;*Ppif*$^{-/-}$;*Sgcd*$^{-/-}$ mice had significantly more mtDNA than *Sgcd*$^{-/-}$ quadricep tissue (fig. S5A). Furthermore, we observed that *Slc25a4*$^{-/-}$;*Ppif*$^{-/-}$;*Sgcd*$^{-/-}$ had more mtDNA than WT quadricep tissue (fig. S5A), suggesting that mitochondrial content is preserved but also expanded in the *Slc25a4*$^{-/-}$;*Ppif*$^{-/-}$;*Sgcd*$^{-/-}$ mice. To assess whether the increase in mtDNA was due to increased mitochondrial biogenesis, we measured peroxisome proliferator-activated receptor-gamma coactivator (PGC)-1α (PGC1α), nuclear respiratory factor 1 (NRF1), and transcription factor A, mitochondrial (TFAM) levels in quadricep tissue lysates, which were not substantially altered between the genotypes examined (fig. S5B). ANT proteins have also been shown to promote PTEN-induced kinase 1 (PINK1)-dependent mitophagy (*41*), hence we also measured markers of mitophagy in isolated muscle mitochondria. We observed that mitochondria from *Slc25a4*$^{-/-}$;*Sgcd*$^{-/-}$ and *Slc25a4*$^{-/-}$;*Ppif*$^{-/-}$;*Sgcd*$^{-/-}$ mice had sharply increased levels of PINK1, PARKIN, and p62 compared to both *Sgcd*$^{-/-}$ and WT mitochondria (fig. S5C). These results are most consistent with impaired mitophagy wherein mitochondria are being marked for degradation but are unable to complete the process, resulting in an accumulation and enlargement of the mitochondrial compartment.

We next assessed whether combined *Slc25a4* and *Ppif* gene deletion improved MD pathology and muscle function. We observed that histopathology in both the diaphragm and quadricep was markedly improved in *Slc25a4*$^{-/-}$;*Ppif*$^{-/-}$;*Sgcd*$^{-/-}$ mice compared with *Sgcd*$^{-/-}$ controls (Fig. 5A). Specifically, regions of active muscle necrosis in *Slc25a4*$^{-/-}$;*Ppif*$^{-/-}$;*Sgcd*$^{-/-}$ mice were not observed, except in rare small, localized instances. Quantification showed that quadriceps from *Slc25a4*$^{-/-}$;*Ppif*$^{-/-}$;*Sgcd*$^{-/-}$ mice had low levels of myofiber central nucleation that were significantly lower than those of both *Sgcd*$^{-/-}$ and *Slc25a4*$^{-/-}$;*Sgcd*$^{-/-}$ mice (Fig. 5B and fig. S5D). Furthermore, muscle from *Slc25a4*$^{-/-}$;*Ppif*$^{-/-}$;*Sgcd*$^{-/-}$ mice had significantly improved myofiber size distribution characterized by a loss of very small regenerating fibers (0 to 20 μm) and a significant preservation of larger fibers (40 to 60 μm) (Fig. 5C), and a near complete loss of Myh3 expression in muscle histological sections, suggesting substantially less necrotic cell death compared with *Sgcd*$^{-/-}$ controls (Fig. 5, D and E). Immunoglobulin M (IgM)–positive myofibers in *Slc25a4*$^{-/-}$;*Ppif*$^{-/-}$;*Sgcd*$^{-/-}$ quadriceps were also not readily observed, indicating a near-complete absence in necrotic myofibers compared in *Sgcd*$^{-/-}$ mice when the genes for ANT1 and CypD were deleted (Fig. 5F). To investigate whole-body muscle damage, we also measured serum levels of muscle creatine kinase (CK) that is released by necrotic muscle fibers in MD. We observed that *Sgcd*$^{-/-}$ mice had significantly elevated levels of serum CK compared to WT mice and that *Slc25a4*$^{-/-}$;*Ppif*$^{-/-}$;*Sgcd*$^{-/-}$ mice had CK levels significantly lower than *Sgcd*$^{-/-}$ mice, comparable to WT controls (Fig. 6A). We also measured muscle performance by downhill treadmill running and observed that *Slc25a4*$^{-/-}$;*Ppif*$^{-/-}$;*Sgcd*$^{-/-}$ mice ran significantly further than *Sgcd*$^{-/-}$ mice and were not statistically different from WT (Fig. 6B and fig. S5E). Isometric force production showed that the TA muscle from *Slc25a4*$^{-/-}$;*Ppif*$^{-/-}$;*Sgcd*$^{-/-}$ rescued the reduction in active force observed in *Sgcd*$^{-/-}$ mice, which was indistinguishable from WT controls (Fig. 6C). These data suggest that the combined *Slc25a4* (ANT1) and *Ppif* (CypD) gene deletion virtually eliminates ongoing necrosis and MD pathology in the *Sgcd*$^{-/-}$ background.

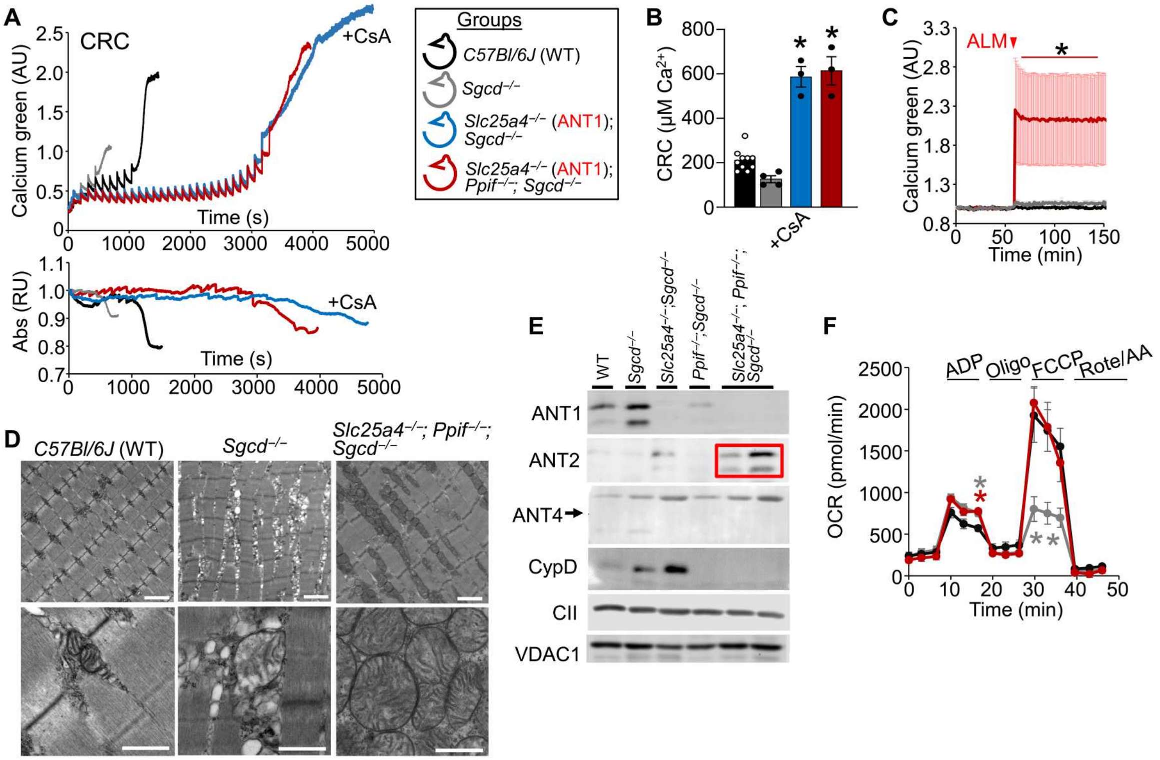

Fig. 4. Combined *Slc25a4* and *Ppif* gene deletion synergistically desensitizes MPTP activity in dystrophic muscle mitochondria. (**A**) Representative CRC assay (top) and parallel absorbance-based mitochondrial swelling (bottom) of quadricep mitochondria from WT, *Sgcd*$^{-/-}$, CsA-treated *Slc25a4*$^{-/-}$;*Sgcd*$^{-/-}$ mice, and *Slc25a4*$^{-/-}$;*Ppif*$^{-/-}$;*Sgcd*$^{-/-}$ mice. Two milligrams of mitochondria was given repetitive 20 μM additions of $CaCl_2$ at each inflection point. The genotypes of mice are color coded in the legend. The *y* axis is arbitrary units or relative units (RU). (**B**) Average CRC measurements of total Ca^{2+} uptake before cessation from quadricep mitochondria of the indicated genotypes of mice. WT *n* = 10; *Sgcd*$^{-/-}$ *n* = 4; *Slc25a4*$^{-/-}$;*Sgcd*$^{-/-}$ + CsA *n* = 3; *Slc25a4*$^{-/-}$;*Ppif*$^{-/-}$;*Sgcd*$^{-/-}$ *n* = 3 (**P* ≤ 0.05 versus *Sgcd*$^{-/-}$). (**C**) Mitochondrial Ca^{2+} assay of quadricep mitochondria from mice of the indicated genotypes. One milligram of mitochondria was treated with 40 μM alamethicin (red arrow). The *y* axis is arbitrary units. WT *n* = 6; *Sgcd*$^{-/-}$ *n* = 3; *Slc25a4*$^{-/-}$;*Ppif*$^{-/-}$;*Sgcd*$^{-/-}$ *n* = 5 (**P* ≤ 0.05 versus WT). (**D**) Representative transmission electron micrographs of quadricep ultrastructure (top) and close-up of mitochondria (bottom) from 8-week-old mice. Scale bars, 2 μm (top) and 800 nm (bottom). (**E**) Western blots from isolated quadricep mitochondria for ANT1, ANT2, ANT4, CypD, VDAC1, and the protein-loading controls (CII in the figure). Red box indicates induction of ANT2. (**F**) Oxygen consumption rate (OCR) of quadricep mitochondria from 8-week-old mice of the indicated genotypes. Respirating mitochondria were treated sequentially with 10 mM adenosine diphosphate (ADP), 2 μM oligomycin (Oligo), 5 μM carbonyl cyanide-*p*-trifluoromethoxyphenylhydrazone (FCCP), and 0.5 μM of a mixture of rotenone and antimycin A (Rote/AA) in a Seahorse bioanalyzer. WT *n* = 4; *Sgcd*$^{-/-}$ *n* = 4; *Slc25a4*$^{-/-}$;*Ppif*$^{-/-}$;*Sgcd*$^{-/-}$ *n* = 4 (**P* ≤ 0.05 versus WT).

DISCUSSION

This study contains direct evidence that ANT is a core MPTP component in mediating necrotic cell death in vivo. *Slc25a4* gene deletion desensitized MPTP activation in isolated diseased muscle mitochondria and markedly reduced MD pathology in vivo. These findings are consistent with a pore-forming role for ANT isoforms in the MPTP that most likely responds to Ca^{2+} overload, although reactive oxygen species generation could also be involved (*42*–*44*), both of which are reported to underlie myofiber loss in MD (*45*, *46*). Our results further demonstrate that ANT proteins function in concert with an unknown CypD-dependent protein species in generating MPTP activity, which we and others have previously proposed on the basis of studies in cells or isolated mitochondria (*14*, *22*). Here, genetically targeting both *Slc25a4* and *Ppif* provides synergistic desensitization of MPTP activation that almost completely prevents necrosis in MD.

It is interesting that deletion of the genes encoding ANT1 and CypD provide some level of sarcolemmal protection compared with *Sgcd*$^{-/-}$ controls even though these animals still lacked the membrane stabilizing δ-sarcoglycan protein. We believe this is due to less mitochondrial dysfunction caused by reduced MPTP activation in these groups, because MPTP activation can generate reactive oxygen species leading to secondary sarcolemmal instability (*47*, *48*). While CsA and its derivative compounds effectively inhibit CypD-dependent MPTP in vivo and are protective in animal models of MD (*5*, *27*–*29*), these agents are needed at high concentrations and can have serious side effects with chronic use (*49*). Our results suggest that ANT inhibitors could also be used as a therapeutic in MD if a nontoxic agent could be identified (*50*). However, another therapeutic strategy could be to combine appropriate CypD and ANT inhibitors, potentially at lower dosages and with synergistic benefits, either independently or in combination with other gene therapy strategies (*51*).

Our results show that *Slc25a4* gene–deleted mice have metabolic dysfunction as observed in previous studies (*32*). Mitochondrial myopathies in humans caused by autosomal dominant mutations in *Slc25a4* are characterized by exercise intolerance and progressive external ophthalmoplegia that manifests in middle age (*39*, *52*, *53*). There are documented cases of humans with homozygous *Slc25a4* loss-of-function mutations that cause childhood exercise

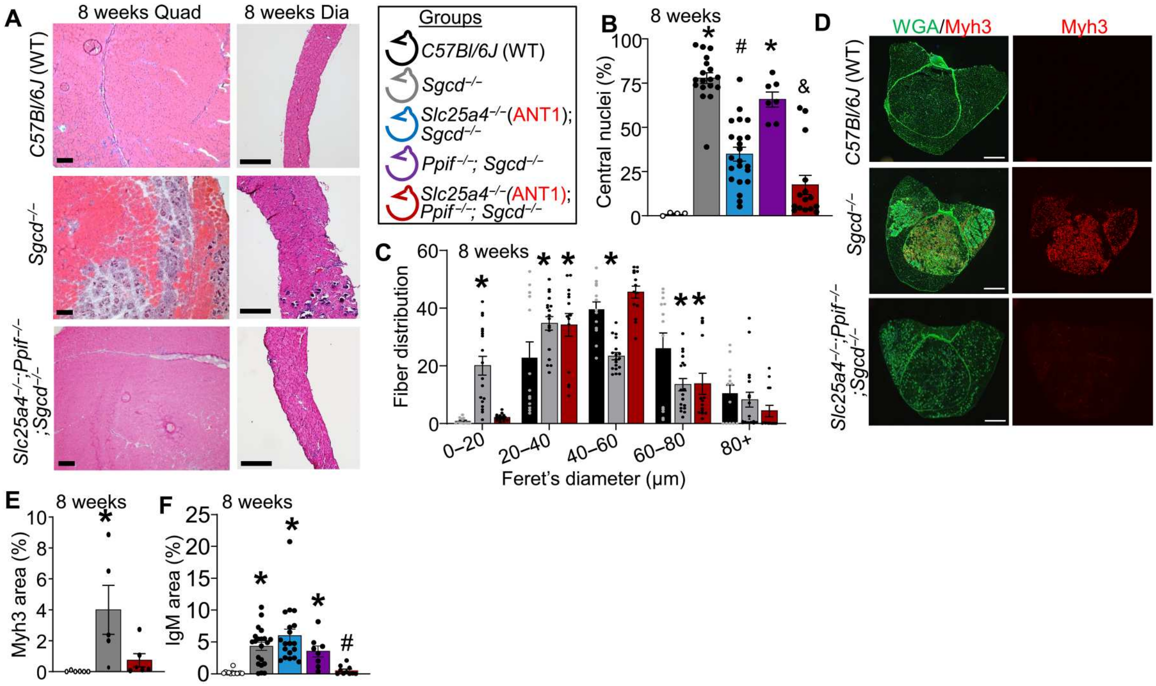

Fig. 5. Combined *Slc25a4* (ANT1) and *Ppif* (CypD) gene deletion prevents tissue histopathology and myofiber necrosis and normalizes muscle function in MD. (**A**) H&E-stained quadricep (left) and diaphragm (right) histological sections from 8-week-old mice of the indicated genotypes. Scale bar, 200 μm. (**B**) Quantification of myofiber central nucleation in quadricep sections from 8-week-old mice with the indicated genotypes by color coding to the legend. WT $n = 4$; *Sgcd*$^{-/-}$ $n = 18$; *Slc25a4*$^{-/-}$;*Sgcd*$^{-/-}$ $n = 22$; *Ppif*$^{-/-}$;*Sgcd*$^{-/-}$ $n = 13$; *Slc25a4*$^{-/-}$;*Ppif*$^{-/-}$;*Sgcd*$^{-/-}$ $n = 15$ (*$P \leq 0.05$ versus WT; #$P \leq 0.05$ versus WT and *Sgcd*$^{-/-}$; &$P \leq 0.05$ versus *Sgcd*$^{-/-}$, *Ppif*$^{-/-}$;*Sgcd*$^{-/-}$, and *Slc25a4*$^{-/-}$;*Sgcd*$^{-/-}$). (**C**) Average Feret's diameter of myofibers measured in quadricep sections from 8-week-old mice of the indicated genotypes. The *y* axis is percentage of total fiber diameters for each genotype up to 100% total. WT $n = 13$; *Sgcd*$^{-/-}$ $n = 18$; *Slc25a4*$^{-/-}$;*Ppif*$^{-/-}$;*Sgcd*$^{-/-}$ $n = 14$ (*$P \leq 0.05$ versus WT). (**D**) Quadricep histological sections immunostained for Myh3 (red) and costained with WGA (green) from 8-week-old mice of the indicated genotypes. Scale bar, 1 mm. (**E**) Quantification of the percent Myh3-positive area in quadricep sections taken from 8-week-old mice of the indicated genotypes. WT $n = 6$; *Sgcd*$^{-/-}$ $n = 5$; *Slc25a4*$^{-/-}$;*Ppif*$^{-/-}$;*Sgcd*$^{-/-}$ $n = 5$ (*$P \leq 0.05$ versus WT). (**F**) Quantification of IgM-positive area in quadricep histological sections taken from 8-week-old mice of the indicated genotypes. WT $n = 13$; *Sgcd*$^{-/-}$ $n = 21$; *Slc25a4*$^{-/-}$;*Sgcd*$^{-/-}$ $n = 19$; *Ppif*$^{-/-}$;*Sgcd*$^{-/-}$ $n = 8$; *Slc25a4*$^{-/-}$;*Ppif*$^{-/-}$;*Sgcd*$^{-/-}$ $n = 10$ (*$P \leq 0.05$ versus WT; #$P \leq 0.05$ versus *Sgcd*$^{-/-}$).

intolerance, mild muscle myopathy, and mild hypertrophic cardiomyopathy, although by 21 and 25 years of age the patients did not yet present with cardiac disease manifestations (*38*, *54*), leaving open the possibility that a properly designed nontoxic ANT1-specific antagonist might offer some therapeutic benefit to skeletal muscle necrotic disease in MD.

ANT proteins can be involved in mitophagy (*41*), and our results provide further evidence for this concept. While more complex experiments that directly assess mitophagic flux are needed, we believe that the increase in muscle mitochondrial content coupled with the increase in mitophagy markers in *Slc25a4*$^{-/-}$;*Sgcd*$^{-/-}$ and *Slc25a4*$^{-/-}$;*Ppif*$^{-/-}$;*Sgcd*$^{-/-}$ mice reflects a deficit in mitophagy wherein mitochondria are marked for degradation by PINK1 but are unable to complete the process and therefore accumulate (Fig. 4D and fig. S5, A to C). The increase in mtDNA is greater in muscle from *Slc25a4*$^{-/-}$;*Ppif*$^{-/-}$;*Sgcd*$^{-/-}$ mice than *Slc25a4*$^{-/-}$;*Sgcd*$^{-/-}$ mice, suggesting the possibility that MPTP activity itself may be important to mitophagy. It has been previously observed that CypD inhibition with CsA can reduce mitophagy in some contexts (*55*–*57*).

Last, results shown here add evidence to the ongoing controversy as to the composition of the MPTP. ANT1 and CypD each separately have some role in facilitating MPTP activity leading to myofiber death in MD. Previous research showed that MPTP has both an ANT-dependent component and an unknown component that requires CypD (*14*). Here, genetically targeting both *Slc25a4* (ANT1) and *Ppif* (CypD) provides synergistic desensitization of MPTP activation that almost completely prevents necrosis in MD. This finding is consistent with previous work and confirms that MPTP either operates by the proposed two-component MPTP model (*19*) or functions by a dual-activation model wherein ANT or CypD are required to activate a single, still unidentified MPTP pore. Another model has been proposed whereby the F_1F_0ATPase can generate MPTP activity in cells and isolated mitochondria (*20*, *21*). However, the concept of the mitochondrial ATPase serving as a direct component of the MPTP in vivo has not been evaluated in a relevant disease setting like MD; thus, the physiologic relevance of the mitochondrial ATPase as a bona fide MPTP component in vivo remains untested.

MATERIALS AND METHODS

Animal models

Germline *Slc25a4*$^{-/-}$ (ANT1 protein), *Ppif*$^{-/-}$ (CypD protein), and *Slc25a31*$^{-/-}$ (ANT4 protein) mice have been described previously (*17*, *32*, *58*). To target the ANT2 encoding gene in a muscle-specific manner, *Slc25a5-LoxP* (fl) allele–targeted mice (*Slc25a5*$^{fl/fl}$) (*13*) were crossed with a line expressing Cre recombinase under the control of the muscle-specific myosin, light polypeptide 1 promoter

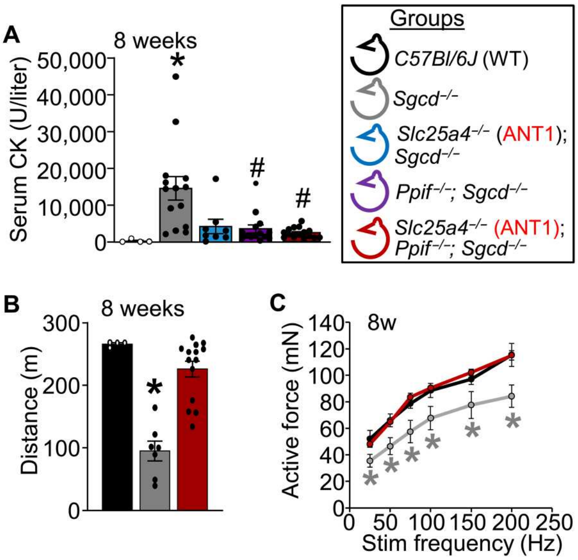

Fig. 6. *Slc25a4* / *Ppif* double-null mice show reduced necrosis and normalized muscle function in MD. (**A**) Serum CK levels for 8-week-old mice of the indicated genotypes. The *y* axis is units of CK per liter of serum. WT *n* = 4; *Sgcd*$^{-/-}$ *n* = 14; *Slc25a4*$^{-/-}$;*Sgcd*$^{-/-}$ *n* = 8; *Ppif*$^{-/-}$;*Sgcd*$^{-/-}$ *n* = 14; *Slc25a4*$^{-/-}$;*Ppif*$^{-/-}$;*Sgcd*$^{-/-}$ *n* = 15 ($*P \leq 0.05$ versus WT; $\#P \leq 0.05$ versus *Sgcd*$^{-/-}$). (**B**) Average treadmill running distance in meters for 8-week-old mice of the indicated genotypes. Maximum possible distance is 270 m. WT *n* = 4; *Sgcd*$^{-/-}$ *n* = 7; *Slc25a4*$^{-/-}$;*Ppif*$^{-/-}$;*Sgcd*$^{-/-}$ *n* = 14 ($*P \leq 0.05$ versus WT). (**C**) Measurement of isometric force in millinewtons generated from the TA muscle of 8-week-old mice with the indicated genotypes. WT *n* = 8; *Sgcd*$^{-/-}$ *n* = 5; *Slc25a4*$^{-/-}$;*Ppif*$^{-/-}$;*Sgcd*$^{-/-}$ *n* = 5 ($*P \leq 0.05$ versus WT).

(*Myl1*$^{tm1(cre)Sjb/J}$) (*59*). The combination of the *Slc25a5*$^{fl/fl}$ alleles with the *Myl1-Cre* line was abbreviated *Slc25a5*^{MKO}. Because both *Slc25a5* and the dystrophin gene (*Dmd*) reside on the X chromosome, we used a δ-sarcoglycan gene–deleted mouse model (*Sgcd*$^{-/-}$) of MD throughout this study (*30*). To assess the effect of deleting the genes encoding ANT1 and CypD in combination, we generated dystrophic mice lacking both genes (*Slc25a4*$^{-/-}$;*Ppif*$^{-/-}$;*Sgcd*$^{-/-}$). To assess the role of different ANT isoforms, we generated dystrophic mice lacking *Slc25a4* and *Slc25a5* (*Slc25a4*$^{-/-}$;*Slc25a5*^{MKO};*Sgcd*$^{-/-}$) or *Slc25a4* and *Slc25a31* (*Slc25a4*$^{-/-}$;*Slc25a31*$^{-/-}$;*Sgcd*$^{-/-}$) by crossing the relevant mouse lines.

All experimental procedures with animals were approved by the Institutional Animal Care and Use Committee of Cincinnati Children's Medical Center, protocols IACUC 2019-0047 and 2021-0047. We have complied with the relevant ethical considerations for animal usage overseen by this committee. The number of mice used in this study reflects the minimum number needed to achieve statistical significance based on experience and previous statistical power analysis. Blinding was performed for some experimental procedures with mice, although blinding was not possible in every instance. Only male mice were used in this study to model the human disease in X-linked Duchenne MD that afflicts primarily males.

Mitochondrial isolation

Quadricep muscle mitochondria were isolated in MS-EGTA buffer [225 mM mannitol, 75 mM sucrose, 5 mM Hepes, and 1 mM EGTA (pH 7.4); Sigma-Aldrich]. Quadricep tissue was minced into 2-mm by 2-mm pieces in 4 ml of MS-EGTAS supplemented with trypsin (0.2 mg/ml; Worthington; 3703; 187 U/mgP) and digested for 5 min. Digestion was stopped by the addition of 10 ml of 0.2% bovine serum albumin (BSA) MS-EGTA. Seven milliliters of the resulting buffer containing the majority of tissue was then homogenized using a glass and Teflon Potter-Elvehjem tissue homogenizer on ice (8 to 15 strokes, depending on the tissue). Tissue homogenates were then subjected to a 2000*g* centrifugation for 5 min (1×), and the supernatants were then centrifuged at 11,500*g* for 10 min. Following centrifugation, mitochondria were suspended in KCl buffer [125 mM KCl, 20 mM Hepes, 2 mM $MgCl_2$, 2 mM KH_2PO_4, and 40 μM EGTA (pH 7.2); Sigma-Aldrich] and either used in a functional assay or spun down (5000*g* for 5 min) and snap frozen in liquid nitrogen for further analysis.

Western blotting

All Western blots were performed using isolated mitochondrial lysates unless otherwise specified in the figure caption. Following mitochondrial isolation, the snap-frozen mitochondrial pellets were suspended in radioimmunoprecipitation assay buffer (RIPA buffer) [10 mM tris-HCl, 150 mM NaCl, 4% glycerol, 0.5 mM NaMetabisulfite, 1% Triton X-100, 0.1% NaDeoxycholate, and 0.05% SDS (pH 7.5); Sigma-Aldrich] containing protease inhibitor cocktails (Roche; 4693124001). The samples were then sonicated and centrifugated to remove the insoluble fraction. The insoluble fractions were discarded following centrifugation. SDS sample buffer [50 mM tris-HCl, 2% SDS, 10% glycerol, 1% β-mercaptoethanol, 12.5 mM EDTA, and 0.02% bromophenol blue (pH 6.8); Sigma-Aldrich] was added to the lysates, and samples were boiled for 5 min. The samples were then loaded onto 10% acrylamide gels and transferred onto polyvinylidene fluoride transfer membranes (MilliporeSigma). For Western blots of whole quadricep, the tissue was snap frozen in liquid nitrogen and then dry homogenized using a chilled mortar and pestle. The resulting muscle homogenate powder was resuspended in RIPA buffer and then treated as above to generate Western samples. The following commercially available primary antibodies were used: *Slc25a4* (ANT1) (Signalway Antibody; 32484; 1:500), *Slc25a5* (ANT2) (Cell Signaling Technology; 14671; 1:500), *Slc25a31* (ANT4) polyclonal antibody (Signalway Antibody; 40596-1; 1:500), *Ppif* (CypD) monoclonal antibody (Affinity BioReagents; PA1-028; 1:1000), PGC1α/β monoclonal antibody (Abcam; ab72230; 1:1000), NRF1 polyclonal antibody (Abcam; ab34682; 1:1000), TFAM polyclonal antibody (Proteintech; 22586-1-AP; 1:1000), PINK1 polyclonal antibody (Cayman Chemical; 10006283; 1:1000), PARKIN monoclonal antibody (Cell Signaling Technology; 4211; 1:1000), p62 polyclonal antibody (Sigma-Aldrich; P0067; 1:1000), MCU monoclonal antibody (Cell Signaling Technology; 14997; 1:1000), MICU1 monoclonal antibody (Cell Signaling Technology; 12524; 1:500), VDAC1 monoclonal antibody (Abcam; ab14734; 1:1000), glyceraldehyde-3-phosphate dehydrogenase monoclonal antibody (Fitzgerald; 0RG109A; 1:5000), and Total OXPHOS rodent WB antibody cocktail (that contained antibodies to electron transport chain complexes 1 to 5; specifically succinate dehydrogenase complex iron-sulfur subunit B from complex II was measured) (Abcam; ab110413; 1:1000). In addition, we used a custom-made MCUb rabbit primary polyclonal antibody (produced by YenZym Antibodies LLC; 1:250) (*36*). Fluorescence-based secondary antibodies were used against different species of antibodies and incubated at room temperature for 1 hour (LI-COR Biosciences; 926-32211 or 925-68070; 1:10,000). Membranes were imaged using an Odyssey CLx Imaging System (LI-COR Biosciences).

Mitochondrial CRC, swelling, and calcium overload assays

The CRC assay and the mitochondrial swelling assay were performed simultaneously using a dual-detector (one to measure fluorescence and the other to measure absorbance), single-cuvette–based fluorimetric system (Horiba Scientific, PTI QM-800). Two milligrams of isolated quadricep mitochondria was loaded into the cuvette along with 250 nM Calcium Green-5 N (Invitrogen; C3737), 7 mM pyruvate (Sigma-Aldrich), and 1 mM malate (Sigma-Aldrich) and brought up to 1 ml using KCl buffer (as above). Mitochondria were then pulsed with sequential additions of $CaCl_2$ (20 μM) until MPTP opening occurred as assessed by mitochondrial Ca^{2+} release and/or swelling.

Calcium overload was measured using the above system and experimental conditions; however mitochondria were suspended in modified KCl buffer lacking EGTA [125 mM KCl, 20 mM Hepes, 2 mM $MgCl_2$, and 2 mM KH_2PO_4 (pH 7.2); Sigma-Aldrich]. To assess free matrix Ca^{2+}, 1 or 2 mg of isolated quadricep mitochondria was treated with a membrane-permeabilizing agent, 40 μM alamethicin (Santa Cruz Biotechnology). The relative amount of matrix Ca^{2+} was assessed by the increase in Calcium Green fluorescence following permeabilization.

Metabolic analysis

OCR was determined using an XF24 Extracellular Flux Analyzer (Agilent Technologies, Seahorse). Isolated quadricep mitochondria (100 μg) were loaded onto XF24 cell culture microplates in KCl buffer containing 7 mM pyruvate (Sigma-Aldrich) and 1 mM malate (Sigma-Aldrich) and subjected to the Mito Stress Test Kit using the standard protocol provided (Agilent Technologies; 103015-100). Briefly, after basal respiration was measured, the mitochondria were treated sequentially with 10 mM adenosine diphosphate (Sigma-Aldrich), 2 μM oligomycin (Agilent Technologies), 5 μM carbonyl cyanide-*p*-trifluoromethoxyphenylhydrazone (Agilent Technologies), and 0.5 μM of a mixture of rotenone and antimycin A (Agilent Technologies).

mtDNA quantification

mtDNA was measured using quantitative polymerase chain reaction (qPCR) methodology (*60*). DNA was isolated from ~10 mg of quadricep tissue using a KingFisher Flex benchtop automated extraction instrument (Thermo Scientific). Briefly, tissue was digested overnight at 55°C in Nuclei Lysis Solution (Promega; PR-A7943) supplemented with 0.1 M EDTA (VWR), Proteinase K (1 mg/ml; Thomas Scientific; C755F45), and RNAse A (2 mg/ml; Qiagen; 19101). To capture nuclear DNA and mtDNA, digested tissue lysates were incubated with MagneSil Paramagnetic Particles (Promega; MD1370) suspended in Lysis Buffer, Blood solution (Promega; PRM1392). DNA-complexed MagneSil PMPs were then loaded into a KingFisher Flex system, washed three times with Alcohol Wash, Blood solution (Promega; MD1412), and eluted into tris-EDTA buffer at pH 8. Isolated quadricep DNA was then diluted to 20 ng/μl, and qPCR was conducted on both *Cox1* to measure mtDNA content (primers: F: 5′-TCTGTTCTGATTCTTTGGGCAC-3′; R: 5′-AGCCAATAGACATTATTGCTCATAC-3′) and *Actb* to measure genomic content (primers: F: 5′-CTGTCGAGTCGCGTCCACC-3′; R: 5′-CAGTGAGGTACTAGCCACGAGA-3′) for each sample using the SsoAdvanced Universal SYBR qPCR Green Supermix reagent (Bio-Rad; 1725274). The qPCR used the following protocol: a 98°C 3-min incubation followed by 40× cycles of 98°C for 15 s and 60°C for 25 s in a Bio-Rad CFX96 Real-Time System Thermocycler (Bio-Rad). mtDNA (*Cox1*) was quantified using the Pffafl method (*61*) with *Atcb* as the reference control gene and then normalized relative to WT levels.

Immunohistochemistry and histological analysis

Histological sections (10 μm) were collected from frozen skeletal muscles using a cryostat. For laminin/IgM staining frozen sections were fixed in 4% paraformaldehyde for 10 min, washed in 1× phosphate buffer saline (1× PBS), and maintained in blocking buffer for 30 min [10% goat serum and 0.4% Triton X diluted in 1× PBS]. Slides were stained overnight at 4°C with antilaminin antibody (Sigma-Aldrich; L9393; 1:200) diluted in staining solution [1% BSA, 0.04% Triton X diluted in 1× PBS]. Slides were then stained with IgM primary antibody conjugated to fluorescein isothiocyanate (Sigma-Aldrich; F9259; 1:100) and Alexa Fluor 568 goat anti-rabbit IgG secondary antibody (Invitrogen, A-11036; 1:300) for 1 hour at room temperature (RT). Nuclei were visualized by a 15-min 4′,6-diamidino-2-phenylindole (DAPI) stain (Invitrogen; D3571; 1:5000). For Myh3 staining, frozen muscle sections were fixed with cold acetone for 10 min, air dried for 30 min, washed with 1× PBS, and blocked with 2% BSA in 1× PBS for 1 hour. Slides were stained overnight at 4°C with anti-Myh3 antibody (Developmental Studies Hybridoma Bank; F1.652, 1:20) diluted in staining solution. Slides were then stained with Alexa Fluor 488 goat anti-mouse IgG1 secondary antibody (Invitrogen; A-21121; 1:400) for 1 hour at RT. Slides were subsequently stained with wheat germ agglutinin (WGA) conjugated to Alexa Fluor 488 (Invitrogen, W11261; 1:200) and DAPI for 20 min to visualize myofiber outlines and nuclei. Immunofluorescence images were captured using a Nikon Eclipse Ti microscope using NIS Elements AR 4.13 software. Regenerating myofibers were assessed by measuring Myh3-positive muscle area from an entire quadricep section at mid-belly. IgM-positive muscle area was assessed from entire quadricep sections taken at the mid-belly of the muscle. All analyses were performed using NIS Elements AR 4.13 software and conducted in a blinded fashion whereby the experimenter was only aware of the genotypes following quantification.

Histological cross sections (10 μm) were collected from quadricep or diaphragm using a cryostat and stained for hematoxylin and eosin to assess mitochondrial muscle myopathy. The rate of myofiber central nucleation was quantified from one 400× magnification micrograph taken from histological sections of the quadricep at the mid-belly. One thousand fibers were measured per quadricep section. The minimal feret′s diameter was determined from laminin-stained whole quadricep muscle using NIS Elements AR 4.13 software. One thousand fibers were measured per quadricep section. All analyses were performed in a blinded fashion whereby the experimenter was only aware of the genotypes following quantification.

Forced treadmill running and EBD uptake

To assess the exercise capacity of mice and sarcolemma stability, mice were subjected to forced treadmill running in the presence of EBD as previously described (*62*). Briefly, adult mice were intraperitoneally injected with EBD (10 mg/ml; 0.1 ml per 10-g body weight) and 24 hours later subjected to forced downhill treadmill running to measure membrane rupture events. Mice were run in an electrically driven six-lane treadmill (Columbus Instruments International; Exer-3/6 Treadmill) at a 5° decline. Mice were given a 10-min training regimen at 6 m/min to familiarize them with the environment and shock grids adjustable from 0 to 2.0 mA. The speed was then increased in increments of 2 m/min every 3 min to a maximum speed of 18 m/min. Exhaustion was assessed as greater than 10 consecutive seconds on the shock grid without attempting to reengage the treadmill which was considered an experimental endpoint. Mice were euthanized 24 hours following the running experiment and isolated muscles were frozen for histological analysis. Histological cross sections (10 μm) were collected from quadricep using a cryostat and subsequently stained with Alexa Fluor 488 WGA and DAPI (as above) for 20 min to visualize myofiber outlines and nuclei, respectively, as described above. Immunofluorescence images were captured using a Nikon Eclipse Ti microscope using NIS Elements AR 4.13 software to determine the percentage of EBD-positive quadricep muscle area. EBD area analysis was performed in a blinded fashion.

Isolated muscle force measurements

Mice were anesthetized by intraperitoneal injection of pentobarbital (6 mg/100 g body weight). The distal tendon of the TA muscle was exposed, and 4-0 nylon suture was tied at the muscle-tendon interface. The knee and foot of the mouse were secured to a platform, and the tendon was mounted to a servomotor (Aurora Scientific; Model 305C). The TA muscle was stimulated using two intramuscular electrodes placed on either side of the peroneal nerve at 200 Hz with a biphase high-power stimulator (Aurora Scientific; Model 701C). Stimulation voltages and optimal muscle length were adjusted to produce maximum isometric twitch force. A series of six consecutive tetanic isometric contractions were performed with a 2-min rest period between each contraction. Specific force was measured by dividing the active force by the muscle's physiologic cross-sectional area, and the percentage drop in force was determined by taking the difference in force between contractions 1 and 6. The experimenter was blinded to the genotypes during the collection of these data.

Transmission electron microscopy

Fresh quadricep was harvested and immediately immersed in relaxing buffer (0.15% sucrose, 5% dextrose, and 100 mM KCl in 1× PBS), subsequently fixed overnight [3.5% glutaraldehyde and 0.15% sucrose in 0.1 M sodium cacodylate (pH 7.4)] and postfixed in 1% OsO_4 (in water) for 2 hours at RT. Samples were then washed, dehydrated and embedded using epoxy resin. Ultrathin sections of tissues were counterstained with 1.5% uranyl acetate, 70% ethanol, and lead nitrate/Na citrate. Images were obtained using a Hitachi 7600 transmission electron microscope connected to an AMT digital camera.

Serum CK measurement

Blood samples from mice were collected from the abdominal aorta of anesthetized mice, and plasma was isolated by centrifugation at 5000*g* for 15 min at 4°C. Serum CK measurement was performed on a Roche Cobas c311 clinical chemistry analyzer (Roche) by a trained observer blinded to genotype.

Statistics

All results are presented as means ± SEM. Data from each experiment was subjected to a Brown-Forsyth test for unequal variance before additional statistical analysis. For datasets with equal variance, statistical analysis was performed with unpaired two-tailed Student's *t* test for two independent groups or one-way analysis of variance (ANOVA) with post hoc Dunnett's test for multiple comparisons of three or more independent groups. Two-way ANOVA with post hoc Dunnett's or Tukey's tests for multiple comparisons were used where appropriate. For datasets with unequal variance, a nonparametric Kruskal-Wallis test was used to assess statistical significance. All statistics were performed using GraphPad Prism 9, and values were considered statistically significant when $P \leq 0.05$. No statistical analysis was used to predetermine sample size although previous power analysis of similar experimental variables in mice did direct selection of group sizes. The experiments were not randomized, and no animals were excluded from analysis. The investigators were not blinded to allocation during all experiments but were blinded in specific experimental outputs as noted. The exact number of animals or biological replicates for each experiment is indicated in the figure legends.

Supplementary Materials

This PDF file includes:

Figs. S1 to S5

REFERENCES AND NOTES

1. D. J. Robichaux, M. Harata, E. Murphy, J. Karch, Mitochondrial permeability transition pore-dependent necrosis. *J. Mol. Cell. Cardiol.* **174**, 47–55 (2023).
2. M. Zoratti, I. Szabo, The mitochondrial permeability transition. *Biochim. Biophys. Acta* **1241**, 139–176 (1995).
3. A. P. Halestrap, A. P. Richardson, The mitochondrial permeability transition: A current perspective on its identity and role in ischaemia/reperfusion injury. *J. Mol. Cell. Cardiol.* **78**, 129–141 (2015).
4. M. R. Alam, D. Baetz, M. Ovize, Cyclophilin D and myocardial ischemia-reperfusion injury: A fresh perspective. *J. Mol. Cell. Cardiol.* **78**, 80–89 (2015).
5. D. P. Millay, M. A. Sargent, H. Osinska, C. P. Baines, E. R. Barton, G. Vuagniaux, H. L. Sweeney, J. Robbins, J. D. Molkentin, Genetic and pharmacologic inhibition of mitochondrial-dependent necrosis attenuates muscular dystrophy. *Nat. Med.* **14**, 442–447 (2008).
6. M. D. Norenberg, K. V. Rao, The mitochondrial permeability transition in neurologic disease. *Neurochem. Int.* **50**, 983–997 (2007).
7. R. A. Quintanilla, C. Tapia, M. J. Perez, Possible role of mitochondrial permeability transition pore in the pathogenesis of Huntington disease. *Biochem. Biophys. Res. Commun.* **483**, 1078–1083 (2017).
8. M. Forte, B. G. Gold, G. Marracci, P. Chaudhary, E. Basso, D. Johnsen, X. Yu, J. Fowlkes, M. Rahder, K. Stem, P. Bernardi, D. Bourdette, Cyclophilin D inactivation protects axons in experimental autoimmune encephalomyelitis, an animal model of multiple sclerosis. *Proc. Natl. Acad. Sci. U.S.A.* **104**, 7558–7563 (2007).
9. H. Du, L. Guo, F. Fang, D. Chen, A. A. Sosunov, G. M. McKhann, Y. Yan, C. Wang, H. Zhang, J. D. Molkentin, F. J. Gunn-Moore, J. P. Vonsattel, O. Arancio, J. X. Chen, S. D. Yan, Cyclophilin D deficiency attenuates mitochondrial and neuronal perturbation and ameliorates learning and memory in Alzheimer's disease. *Nat. Med.* **14**, 1097–1105 (2008).
10. L. J. Martin, B. Gertz, Y. Pan, A. C. Price, J. D. Molkentin, Q. Chang, The mitochondrial permeability transition pore in motor neurons: Involvement in the pathobiology of ALS mice. *Exp. Neurol.* **218**, 333–346 (2009).
11. A. P. Halestrap, A. M. Davidson, Inhibition of $Ca2^+$-induced large-amplitude swelling of liver and heart mitochondria by cyclosporin is probably caused by the inhibitor binding to mitochondrial-matrix peptidyl-prolyl cis-trans isomerase and preventing it interacting with the adenine nucleotide translocase. *Biochem. J.* **268**, 153–160 (1990).
12. N. Brustovetsky, M. Tropschug, S. Heimpel, D. Heidkamper, M. Klingenberg, A large Ca^{2+}–dependent channel formed by recombinant ADP/ATP carrier from Neurospora

crassa resembles the mitochondrial permeability transition pore. *Biochemistry* **41**, 11804–11811 (2002).
13. J. E. Kokoszka, K. G. Waymire, S. E. Levy, J. E. Sligh, J. Cai, D. P. Jones, G. R. MacGregor, D. C. Wallace, The ADP/ATP translocator is not essential for the mitochondrial permeability transition pore. *Nature* **427**, 461–465 (2004).
14. J. Karch, M. J. Bround, H. Khalil, M. A. Sargent, N. Latchman, N. Terada, P. M. Peixoto, J. D. Molkentin, Inhibition of mitochondrial permeability transition by deletion of the ANT family and CypD. *Sci. Adv.* **5**, eaaw4597 (2019).
15. C. P. Baines, R. A. Kaiser, N. H. Purcell, N. S. Blair, H. Osinska, M. A. Hambleton, E. W. Brunskill, M. R. Sayen, R. A. Gottlieb, G. W. Dorn, J. Robbins, J. D. Molkentin, Loss of cyclophilin D reveals a critical role for mitochondrial permeability transition in cell death. *Nature* **434**, 658–662 (2005).
16. E. Basso, L. Fante, J. Fowlkes, V. Petronilli, M. A. Forte, P. Bernardi, Properties of the permeability transition pore in mitochondria devoid of Cyclophilin D. *J. Biol. Chem.* **280**, 18558–18561 (2005).
17. T. Nakagawa, S. Shimizu, T. Watanabe, O. Yamaguchi, K. Otsu, H. Yamagata, H. Inohara, T. Kubo, Y. Tsujimoto, Cyclophilin D-dependent mitochondrial permeability transition regulates some necrotic but not apoptotic cell death. *Nature* **434**, 652–658 (2005).
18. A. C. Schinzel, O. Takeuchi, Z. Huang, J. K. Fisher, Z. Zhou, J. Rubens, C. Hetz, N. N. Danial, M. A. Moskowitz, S. J. Korsmeyer, Cyclophilin D is a component of mitochondrial permeability transition and mediates neuronal cell death after focal cerebral ischemia. *Proc. Natl. Acad. Sci. U.S.A.* **102**, 12005–12010 (2005).
19. M. J. Bround, D. M. Bers, J. D. Molkentin, A 20/20 view of ANT function in mitochondrial biology and necrotic cell death. *J. Mol. Cell. Cardiol.* **144**, A3–A13 (2020).
20. V. Giorgio, S. von Stockum, M. Antoniel, A. Fabbro, F. Fogolari, M. Forte, G. D. Glick, V. Petronilli, M. Zoratti, I. Szabo, G. Lippe, P. Bernardi, Dimers of mitochondrial ATP synthase form the permeability transition pore. *Proc. Natl. Acad. Sci. U.S.A.* **110**, 5887–5892 (2013).
21. K. N. Alavian, G. Beutner, E. Lazrove, S. Sacchetti, H. A. Park, P. Licznerski, H. Li, P. Nabili, K. Hockensmith, M. Graham, G. A. Porter Jr., E. A. Jonas, An uncoupling channel within the c-subunit ring of the F1FO ATP synthase is the mitochondrial permeability transition pore. *Proc. Natl. Acad. Sci. U.S.A.* **111**, 10580–10585 (2014).
22. M. A. Neginskaya, M. E. Solesio, E. V. Berezhnaya, G. F. Amodeo, N. Mnatsakanyan, E. A. Jonas, E. V. Pavlov, ATP synthase C-subunit-deficient mitochondria have a small cyclosporine A-sensitive channel, but lack the permeability transition pore. *Cell Rep.* **26**, 11–17.e2 (2019).
23. A. Carrer, L. Tommasin, J. Sileikyte, F. Ciscato, R. Filadi, A. Urbani, M. Forte, A. Rasola, I. Szabo, M. Carraro, P. Bernardi, Defining the molecular mechanisms of the mitochondrial permeability transition through genetic manipulation of F-ATP synthase. *Nat. Commun.* **12**, 4835 (2021).
24. A. Caudal, X. Tang, J. D. Chavez, A. Keller, J. P. Mohr, A. A. Bakhtina, O. Villet, H. Chen, B. Zhou, M. A. Walker, R. Tian, J. E. Bruce, Mitochondrial interactome quantitation reveals structural changes in metabolic machinery in the failing murine heart. *Nat. Cardiovasc. Res.* **1**, 855–866 (2022).
25. P. Podkalicka, O. Mucha, J. Dulak, A. Loboda, Targeting angiogenesis in Duchenne muscular dystrophy. *Cell. Mol. Life Sci.* **76**, 1507–1528 (2019).
26. F. Rahimov, L. M. Kunkel, The cell biology of disease: Cellular and molecular mechanisms underlying muscular dystrophy. *J. Cell Biol.* **201**, 499–510 (2013).
27. E. R. Wissing, D. P. Millay, G. Vuagniaux, J. D. Molkentin, Debio-025 is more effective than prednisone in reducing muscular pathology in mdx mice. *Neuromuscul. Disord.* **20**, 753–760 (2010).
28. E. Palma, T. Tiepolo, A. Angelin, P. Sabatelli, N. M. Maraldi, E. Basso, M. A. Forte, P. Bernardi, P. Bonaldo, Genetic ablation of cyclophilin D rescues mitochondrial defects and prevents muscle apoptosis in collagen VI myopathic mice. *Hum. Mol. Genet.* **18**, 2024–2031 (2009).
29. A. Zulian, E. Rizzo, M. Schiavone, E. Palma, F. Tagliavini, B. Blaauw, L. Merlini, N. M. Maraldi, P. Sabatelli, P. Braghetta, P. Bonaldo, F. Argenton, P. Bernardi, NIM811, a cyclophilin inhibitor without immunosuppressive activity, is beneficial in collagen VI congenital muscular dystrophy models. *Hum. Mol. Genet.* **23**, 5353–5363 (2014).
30. A. A. Hack, M. Y. Lam, L. Cordier, D. I. Shoturma, C. T. Ly, M. A. Hadhazy, M. R. Hadhazy, H. L. Sweeney, E. M. McNally, Differential requirement for individual sarcoglycans and dystrophin in the assembly and function of the dystrophin-glycoprotein complex. *J. Cell Sci.* **113**, 2535–2544 (2000).
31. M. V. Dubinin, E. Y. Talanov, K. S. Tenkov, V. S. Starinets, I. B. Mikheeva, M. G. Sharapov, K. N. Belosludtsev, Duchenne muscular dystrophy is associated with the inhibition of calcium uniport in mitochondria and an increased sensitivity of the organelles to the calcium-induced permeability transition. *Biochim. Biophys. Acta Mol. Basis Dis.* **1866**, 165674 (2020).
32. B. H. Graham, K. G. Waymire, B. Cottrell, I. A. Trounce, G. R. MacGregor, D. C. Wallace, A mouse model for mitochondrial myopathy and cardiomyopathy resulting from a deficiency in the heart/muscle isoform of the adenine nucleotide translocator. *Nat. Genet.* **16**, 226–234 (1997).
33. S. E. Levy, Y. S. Chen, B. H. Graham, D. C. Wallace, Expression and sequence analysis of the mouse adenine nucleotide translocase 1 and 2 genes. *Gene* **254**, 57–66 (2000).
34. J. E. Kokoszka, K. G. Waymire, A. Flierl, K. M. Sweeney, A. Angelin, G. R. MacGregor, D. C. Wallace, Deficiency in the mouse mitochondrial adenine nucleotide translocator isoform 2 gene is associated with cardiac noncompaction. *Biochim. Biophys. Acta* **1857**, 1203–1212 (2016).
35. A. Raffaello, D. De Stefani, D. Sabbadin, E. Teardo, G. Merli, A. Picard, V. Checchetto, S. Moro, I. Szabo, R. Rizzuto, The mitochondrial calcium uniporter is a multimer that can include a dominant-negative pore-forming subunit. *EMBO J.* **32**, 2362–2376 (2013).
36. J. Huo, S. Lu, J. Q. Kwong, M. J. Bround, K. M. Grimes, M. A. Sargent, M. E. Brown, M. E. Davis, D. M. Bers, J. D. Molkentin, MCUb induction protects the heart from postischemic remodeling. *Circ. Res.* **127**, 379–390 (2020).
37. M. Paillard, G. Csordas, G. Szanda, T. Golenar, V. Debattisti, A. Bartok, N. Wang, C. Moffat, E. L. Seifert, A. Spat, G. Hajnoczky, Tissue-specific mitochondrial decoding of cytoplasmic Ca^{2+} signals is controlled by the stoichiometry of MICU1/2 and MCU. *Cell Rep.* **18**, 2291–2300 (2017).
38. L. Palmieri, S. Alberio, I. Pisano, T. Lodi, M. Meznaric-Petrusa, J. Zidar, A. Santoro, P. Scarcia, F. Fontanesi, E. Lamantea, I. Ferrero, M. Zeviani, Complete loss-of-function of the heart/muscle-specific adenine nucleotide translocator is associated with mitochondrial myopathy and cardiomyopathy. *Hum. Mol. Genet.* **14**, 3079–3088 (2005).
39. B. Clemencon, M. Babot, V. Trezeguet, The mitochondrial ADP/ATP carrier (SLC25 family): Pathological implications of its dysfunction. *Mol. Aspects Med.* **34**, 485–493 (2013).
40. J. W. Elrod, R. Wong, S. Mishra, R. J. Vagnozzi, B. Sakthievel, S. A. Goonasekera, J. Karch, S. Gabel, J. Farber, T. Force, J. H. Brown, E. Murphy, J. D. Molkentin, Cyclophilin D controls mitochondrial pore-dependent Ca^{2+} exchange, metabolic flexibility, and propensity for heart failure in mice. *J. Clin. Invest.* **120**, 3680–3687 (2010).
41. A. Hoshino, W. J. Wang, S. Wada, C. McDermott-Roe, C. S. Evans, B. Gosis, M. P. Morley, K. S. Rathi, J. Li, K. Li, S. Yang, M. J. McManus, C. Bowman, P. Potluri, M. Levin, S. Damrauer, D. C. Wallace, E. L. F. Holzbaur, Z. Arany, The ADP/ATP translocase drives mitophagy independent of nucleotide exchange. *Nature* **575**, 375–379 (2019).
42. H. Aquila, M. Klingenberg, The reactivity of -SH groups in the ADP/ATP carrier isolated from beef heart mitochondria. *Eur. J. Biochem.* **122**, 141–145 (1982).
43. A. P. Halestrap, K. Y. Woodfield, C. P. Connern, Oxidative stress, thiol reagents, and membrane potential modulate the mitochondrial permeability transition by affecting nucleotide binding to the adenine nucleotide translocase. *J. Biol. Chem.* **272**, 3346–3354 (1997).
44. G. P. McStay, S. J. Clarke, A. P. Halestrap, Role of critical thiol groups on the matrix surface of the adenine nucleotide translocase in the mechanism of the mitochondrial permeability transition pore. *Biochem. J.* **367**, 541–548 (2002).
45. A. R. Burr, J. D. Molkentin, Genetic evidence in the mouse solidifies the calcium hypothesis of myofiber death in muscular dystrophy. *Cell Death Differ.* **22**, 1402–1412 (2015).
46. J. R. Terrill, H. G. Radley-Crabb, T. Iwasaki, F. A. Lemckert, P. G. Arthur, M. D. Grounds, Oxidative stress and pathology in muscular dystrophies: Focus on protein thiol oxidation and dysferlinopathies. *FEBS J.* **280**, 4149–4164 (2013).
47. D. B. Zorov, M. Juhaszova, S. J. Sollott, Mitochondrial reactive oxygen species (ROS) and ROS-induced ROS release. *Physiol. Rev.* **94**, 909–950 (2014).
48. D. G. Allen, N. P. Whitehead, S. C. Froehner, Absence of dystrophin disrupts skeletal muscle signaling: Roles of Ca^{2+}, reactive oxygen species, and nitric oxide in the development of muscular dystrophy. *Physiol. Rev.* **96**, 253–305 (2016).
49. A. G. Palestine, R. B. Nussenblatt, C. C. Chan, Side effects of systemic cyclosporine in patients not undergoing transplantation. *Am. J. Med.* **77**, 652–656 (1984).
50. W. Welling, J. A. Cohen, W. Berends, Disturbance of oxidative phosphorylation by an antibioticum produced by Pseudomonas cocovenenans. *Biochem. Pharmacol.* **3**, 122–135 (1960).
51. J. M. Crudele, J. S. Chamberlain, AAV-based gene therapies for the muscular dystrophies. *Hum. Mol. Genet.* **28**, R102–R107 (2019).
52. H. Komaki, T. Fukazawa, H. Houzen, K. Yoshida, I. Nonaka, Y. Goto, A novel D104G mutation in the adenine nucleotide translocator 1 gene in autosomal dominant progressive external ophthalmoplegia patients with mitochondrial DNA with multiple deletions. *Ann. Neurol.* **51**, 645–648 (2002).
53. K. P. Park, H. S. Kim, E. S. Kim, Y. E. Park, C. H. Lee, D. S. Kim, SLC25A4 and C10ORF2 mutations in autosomal dominant progressive external ophthalmoplegia. *J. Clin. Neurol.* **7**, 25–30 (2011).
54. A. Echaniz-Laguna, M. Chassagne, J. Ceresuela, I. Rouvet, S. Padet, C. Acquaviva, S. Nataf, S. Vinzio, D. Bozon, B. Mousson de Camaret, Complete loss of expression of the ANT1 gene causing cardiomyopathy and myopathy. *J. Med. Genet.* **49**, 146–150 (2012).
55. R. S. Carreira, Y. Lee, M. Ghochani, A. B. Gustafsson, R. A. Gottlieb, Cyclophilin D is required for mitochondrial removal by autophagy in cardiac cells. *Autophagy* **6**, 462–472 (2010).

56. A. Rodriguez-Hernandez, M. D. Cordero, L. Salviati, R. Artuch, M. Pineda, P. Briones, L. Gomez Izquierdo, D. Cotan, P. Navas, J. A. Sanchez-Alcazar, Coenzyme Q deficiency triggers mitochondria degradation by mitophagy. *Autophagy* **5**, 19–32 (2009).
57. S. Rodriguez-Enriquez, Y. Kai, E. Maldonado, R. T. Currin, J. J. Lemasters, Roles of mitophagy and the mitochondrial permeability transition in remodeling of cultured rat hepatocytes. *Autophagy* **5**, 1099–1106 (2009).
58. J. V. Brower, N. Rodic, T. Seki, M. Jorgensen, N. Fliess, A. T. Yachnis, J. R. McCarrey, S. P. Oh, N. Terada, Evolutionarily conserved mammalian adenine nucleotide translocase 4 is essential for spermatogenesis. *J. Biol. Chem.* **282**, 29658–29666 (2007).
59. G. W. Bothe, J. A. Haspel, C. L. Smith, H. H. Wiener, S. J. Burden, Selective expression of Cre recombinase in skeletal muscle fibers. *Genesis* **26**, 165–166 (2000).
60. A. M. Andres, K. C. Tucker, A. Thomas, D. J. Taylor, D. Sengstock, S. M. Jahania, R. Dabir, S. Pourpirali, J. A. Brown, D. G. Westbrook, S. W. Ballinger, R. M. Mentzer Jr., R. A. Gottlieb, Mitophagy and mitochondrial biogenesis in atrial tissue of patients undergoing heart surgery with cardiopulmonary bypass. *JCI Insight* **2**, e89303 (2017).
61. M. W. Pfaffl, A new mathematical model for relative quantification in real-time RT-PCR. *Nucleic Acids Res.* **29**, e45 (2001).
62. S. A. Goonasekera, C. K. Lam, D. P. Millay, M. A. Sargent, R. J. Hajjar, E. G. Kranias, J. D. Molkentin, Mitigation of muscular dystrophy in mice by SERCA overexpression in skeletal muscle. *J. Clin. Invest.* **121**, 1044–1052 (2011).

Acknowledgments

Funding: This work was supported by National Heart, Lung, and Blood Institutes of the NIH grant R01HL132831 (J.D.M.), National Institute of Arthritis and Musculoskeletal and Skin Diseases of the NIH grant K99AR078253 (M.J.B.), National Heart, Lung, and Blood Institutes of the NIH grant R01HL150031 (J.K.), L. B. Research and Education Foundation (J.R.H.), and Leducq Fondation funding (J.D.M.). **Author contributions:** Conceptualization: M.J.B., J.K., and J.D.M. Methodology: M.J.B. and J.D.M. Investigation: M.J.B., J.R.H., A.J.Y., and M.A.S. Visualization: M.J.B., J.R.H., M.A.S., and J.D.M. Supervision: J.D.M. Writing—original draft: M.J.B. and J.D.M. Writing—review and editing: M.J.B. and J.D.M. **Competing interests:** The authors declare that they have no competing interests. **Data and materials availability:** All data needed to evaluate the conclusions in the paper are present in the paper and/or the Supplementary Materials. The ANT gene-targeted mice used here were provided by D. Wallace of the Children's Hospital of Philadelphia [see (*13*)] under a material transfer agreement, and he should be contacted for their availability pending scientific review and completing a material transfer agreement with his institution.

Submitted 14 April 2023
Accepted 26 July 2023
Published 25 August 2023
10.1126/sciadv.adi2767